Volume 17
Number 6
14 February 2025
Pages 2915-3520

Nanoscale

rsc.li/nanoscale

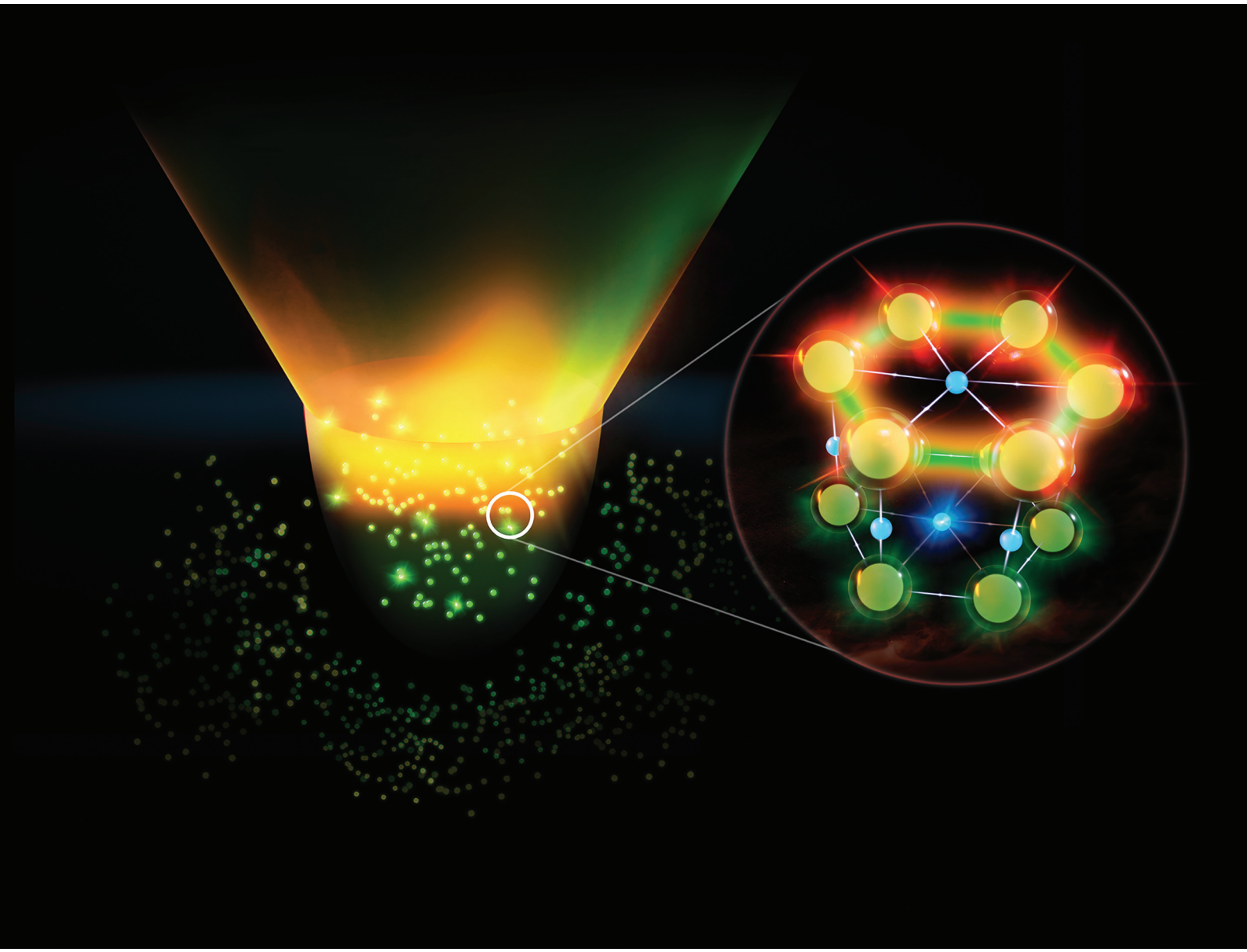

ISSN 2040-3372

ROYAL SOCIETY OF CHEMISTRY

PAPER
Ernesto Jiménez-Villar *et al.*
Strong enhancement of effective refractive index in structured colloids (TiO_2@Silica): Localization of light

NCNST

Nanoscale

ROYAL SOCIETY OF CHEMISTRY

PAPER

View Article Online
View Journal | View Issue

Cite this: *Nanoscale*, 2025, **17**, 3061

Strong enhancement of effective refractive index in structured colloids (TiO_2@Silica): Localization of light†

Jessica Dipold,[a] Niklaus U. Wetter,[a] Francisco C. Marques,[b] Aristide Dogariu [c] and Ernesto Jiménez-Villar *[b,c]

Received 4th September 2024,
Accepted 11th December 2024

DOI: 10.1039/d4nr03626c

rsc.li/nanoscale

We use non-resonant Raman scattering to demonstrate a large enhancement of the effective refractive index experienced by Raman photons in a scattering medium comprising spatially-correlated photonic structures of core–shell TiO_2@Silica scatterers mixed with silica nanoparticles and suspended in ethanol. We show that the high refractive index extends outside the physical boundary of the medium, which is attributed to the evanescent contributions of electromagnetic modes that are strongly localized within the medium. Notably, the effective enhancement can be observed even at very low intensities of Raman emission. This anomalous non-linear phenomenon could be explained by the successive polarization of valence electrons to virtual states induced by the strong photon correlations in the strongly localized electromagnetic modes. The enhancement of refractive index and its extension in the vicinity of the medium's interface provide new opportunities for controlling the electromagnetic fields in advanced photonic devices.

Introduction

The enhancement of the light–matter coupling in dielectric-scattering media, in addition to delving into fundamental concepts of physics, can also present advanced applications.[1–3] In recent years, dramatic progress in the photonics field in engineered-disordered media has been seen.[1,4–7] Engineered or correlated disorder in photonic assemblies can yield anomalous and impactful optical phenomena such as localization of light, enhanced light–matter interaction, unidirectional invisibility and single mode lasing. Several works on these topics have been published elsewhere.[1,8–11] In particular, localization of light in a three-dimensional (3D) dielectric system shows prospects for completely new optical phenomena.[2,3] However, it has proven elusive,[12–16] which has led to extensive debate.[17] Absorption, non-linear phenomena and the near field dipole–dipole coupling were claimed to hamper localization of light. In fact, renormalization of the absorption coefficient (enhanced absorption) in a disordered scattering medium at the mobility edge was first predicted theoretically[18] and later experimentally shown.[19] In our recent works,[1,4,5] we showed that the correlation in the scatterers' position, due to the Coulomb interaction between scatterers, might give rise to strongly localized electromagnetic modes (localization of light) and associated phenomena, such as strong enhancement of the Raman scattering cross section and very low random lasing threshold. The latter have been observed in correlated colloidal structures composed of core–shell TiO_2@Silica scatterers suspended in ethanol with or without addition of silica nanoparticles.[1,4,5] The silica NPs (20 nm diameter) enhances the particle–particle interaction between the TiO_2@Silica NPs (scatterers). These silica NPs should be localized at the intermediate regions between TiO_2@Silica NPs, due to their higher mobility and the strong Coulomb repulsion exerted on them by the larger TiO_2@Silica NPs (500 nm diameter). In addition, due to the high dielectric permittivity of silica NPs,[20] an increase in the solvation layer, effective viscosity and Coulomb potential is expected in the intermediate region between TiO_2@Silica NPs,[21] favoring the scatterer–scatterer interaction and, therefore, the correlation in their positions. Consequently, silica NPs would act like pivots or bridges for the Coulomb interaction between TiO_2@Silica NPs.

In this work, through non-resonant Raman scattering, strong enhancement of the effective refractive index experienced by Raman photons at the sample input interface is shown in a

[a]*Instituto de pesquisas Energéticas e Nucleares, CNEN_IPEN, São Paulo, SP 05508-000, Brazil*
[b]*Instituto de Física "Gleb Wataghin", Universidade Estadual de Campinas, Campinas, SP 13083-859, Brazil. E-mail: Ernesto.jimenez@uv.es*
[c]*CREOL, The College of Optics and Photonics, University of Central Florida, Orlando, FL 32816, USA*

†Electronic supplementary information (ESI) available: Theoretical description of the TiO_2@Silica Coulomb interaction in the colloidal suspension; description of the Raman measurement setups and Raman emission spectra; mathematical description for the Raman signal correction by pumping and collection depth; the effective refractive indexes of the sapphire and glass slides at the sample–slide interface extracted from measurements; schematic description of the flow of operations executed to determine the effective refractive indexes. See DOI: https://doi.org/10.1039/d4nr03626c

TiO_2@Silica ethanol suspension with addition of silica NPs, which was suggested[1,4,19,22,23] and inferred[24,25] in our previous works. This strong enhancement of the effective refractive index experienced by Raman photons represents a new kind of non-linear phenomenon, especially considering the low intensities involved in the Raman emission. In previous works, we showed strong enhancement in the Raman cross section (non-resonant)[1,4] and absorption coefficient[19,24,25] near the sample input interface. The enhancement of the non-resonant Raman scattering together with an enhanced absorption should also imply an increase in the effective refractive index (n_S). It should be noted that according to the Kramers–Kronig relationship, an enhanced absorption should be linked to an enhancement of the refractive index. Additionally, an enhancement of the non-resonant Raman scattering should be a consequence of the increase in the polarization of valence electrons to virtual states, which, in turn, leads to an increase in the refractive index. A parallel of this phenomenon in electronic systems was first addressed by Campagnano and Nazarov, who proposed a dynamic barrier at the border of a disordered electronic medium at localization.[26]

Materials and methods

Core–shell TiO_2@Silica NPs, synthesized by an improved Stöber method,[19] were dispersed in ethanol (HPLC) solution with the TiO_2 core (rutile) with filling fractions (FF_{TiO_2}) of 0.26%, 0.54%, 1.35%, 4.8%, 8.8% and 12.1%. Additionally, silica NPs (20 nm diameter) with filling fractions (FF_{SiO_2}) of 0.75% and 1.5% were added to these TiO_2@Silica NP suspensions. The TiO_2@Silica NPs used in the current experiments are the same as those used in our previous reports.[1,4,5,19,22–25] TEM, EELS (electron energy loss spectroscopy) mapping (Si) and energy dispersive X-ray fluorescence (ED-XRF) spectroscopy of the core–shell TiO_2@Silica NPs were performed and reported in our previous work.[4,19] The mass percentage ratio (Ti/Si), determined by ED-XRF, was Ti_{72}/Si_{28}, which allows estimating a silica shell thickness of ~40–45 nm. Diffraction patterns from the TiO_2@Silica suspensions showing the correlation of the scatterers' position can be found in our previous works.[5,27] Details of the synthesis of TiO_2@Silica NPs can be found in the ESI.†

A Micro-Raman LabRAMAN HR Horiba Scientific with a CW 532 nm laser as an excitation source (50 mW with power fluctuation ± 1%) was used for Raman scattering measurements. Micro-Raman measurements were done using a Leica 50× objective with the numerical aperture NA = 0.55. A schematic diagram of the Raman measurement can be found in our previous works.[1,4] Three arrangements were performed, one without using slides to cover the sample (air) and the other two using either glass (refractive index for BK7 is n_{Glass} = 1.52) or sapphire ($n_{Al_2O_3}$ = 1.78) slides to cover the sample. For these air, glass and sapphire (slide) arrangements, the pumping spot sizes were 0.8 μm, 1.2 μm and 1.4 μm, respectively. The latter represents pumping power densities of 10×10^{10} W m^{-2}, 4.4×10^{10} W m^{-2} and 3.2×10^{10} W m^{-2} for the air, glass and sapphire (slide) arrangements, respectively. For the above three arrangements, the Raman signature of the TiO_2 core (rutile, 410 nm mean diameter) was monitored as a function of FF_{TiO_2}.

Fig. 1 shows illustrations of Raman pumping and collection corresponding to the three setups used for collecting the Raman signal and studying the enhancement of the effective refractive index at the sample–slide interface with air, glass and sapphire as cover slides (from left to right). For pumping and collection of the Raman signal, θ_{CAir}, θ_{CGlass}, $\theta_{CAl_2O_3}$ cone angles and the depth of focus ($d_{B(M)}$) are only determined by the classical refractive indexes of slides, n_{CM} (n_{CAir}, n_{CGlass}, $n_{CAl_2O_3}$) and the numerical aperture (NA) of the pumping-collection objective, NA = 0.55. The pumping-collection depth ($d_{B(M)}$) is calculated through $d_{B(M)} = \frac{\lambda \times n_{CM}}{NA^2}$, where λ = 532 nm is the pumping wavelength, n_{CM} is the refractive index of the slide and NA = 0.55 is the numerical aperture of the

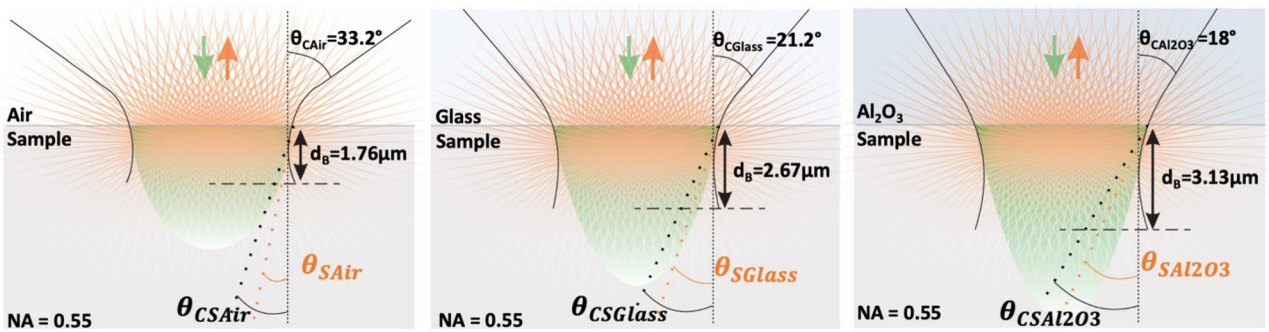

Fig. 1 Illustrations of Raman pumping and collection using the 50× objective and air, glass and sapphire (Al_2O_3) slides (from left to right). The green and orange arrows represent the pumping and Raman emission, respectively. An enhancement in the effective refractive index of the sample leads to a decrease in the Raman cone angle (θ_{SAir}, θ_{SGlass}, $\theta_{SAl_2O_3}$) collected by each detection system (air, glass and sapphire). θ_{CSAir}, $\theta_{CSGlass}$ and $\theta_{CSAl_2O_3}$ are the classical Raman cone angles of pumping by each setup and would also be the collected angle if the effective refractive index of the sample was not enhanced. θ_{CAir}, θ_{CGlass} and $\theta_{CAl_2O_3}$ are the angles of the entry and collection cone (Raman) at the air–sample or air–slide interfaces, which determine the pump and collection depth into the sample (d_B). These angles are insensitive to the dynamics of the refractive indexes of the sample and the slide at the sample–slide interface.

objective. More details about the Raman measurements can be found in the ESI.†

Results

An enhancement in the effective refractive index of the sample (n_S) at the sample–slide interface, experienced by Raman photons, should induce a reduction of the cone angle of the Raman signal collected from the sample (θ_{SAir}, θ_{SGlass}, $\theta_{SAl_2O_3}$; Fig. 1), due to light refraction at the sample–slide or sample–air interfaces. In turn, an increase of the internal reflection is also expected at these interfaces, which would reduce the Raman signal collected. This n_S (sample) enhancement at the sample–slide interface could be extended to the refractive index of slides (sapphire and glass), due to the interaction with the evanescent wave coming from the electromagnetic modes strongly localized in the sample near the input interface (sample–slide). For the measurement without a slide (air), the enhancement of refractive index of air at the sample–air interface through the interaction with the evanescent wave would not be noticeable, since the electric susceptibility of air (χ_{eAir}) is close to zero, so the enhanced χ_{eAir} value would also be close to zero ($n_{Air} = \sqrt{1+\chi_{eAir}}$). Therefore, an n_S enhancement for the measurement without a slide (air) should result in a lower collected Raman signal than expected without n_S enhancement, since an enhanced n_S would lead to an increase in the n_S/n_{Air} contrast at the sample–air interface, inducing a reduction in the Raman collection angle by refraction and an increase in the internal reflection. Following the above arguments, we could demonstrate an increase of the effective refractive index of the sample (n_S) experienced by Raman photons at the sample–slide interface for $FF_{TiO_2} > 0.26\%$.

The Raman signal, measured experimentally (I_{Exp}) for each arrangement (air and slides), is plotted as a function of FF_{TiO_2} for both FF_{SiO_2} (Fig. 2a and b). As shown for the three arrangements, the Raman signal increases quicker than linearly as the FF_{TiO_2} is increased. The solid red, black and blue lines represent the expected linear behavior of the Raman signal in FF_{TiO_2} for the air, glass and sapphire arrangements, respectively.

The strongest Raman signal is collected for the air arrangement. This can be associated with the small spot size and depth of focus (higher numerical aperture) compared to the other arrangements (sapphire and glass slides), leading to an increase in the pumping power density per unit volume. The faster than linear increase in the Raman signal in FF_{TiO_2} represents a per-particle enhanced Raman scattering cross section.

Conventionally, the Raman signal must be proportional to both the emitter concentration (FF_{TiO_2}) and excitation intensity. The enhancement of the Raman signal or Raman scattering cross section per particle as a function of FF_{TiO_2}, determined by normalizing the Raman signal by FF_{TiO_2} and by the Raman signal at $FF_{TiO_2} = 0.26\%$, is illustrated in Fig. 2c and d. Even though the Raman signal is higher for the air arrangement (no slide), the enhancement in the Raman signal is stronger for the glass slide arrangement. This is the consequence of the index matching at the sample–glass interface, which would reduce the collection losses by internal reflection caused by an n_S enhancement at the sample–glass interface. We also note that the experimental setup (50× objective with NA = 0.55) allows a collection depth ($d_{B(M)}$) that is strongly sensitive to the pumping arrangement (sapphire and glass slides, and air). Therefore, for a better comparison of the enhancement as a function of FF_{TiO_2}, one needs a correction of the Raman intensity considering the pumping and collection depths, particularly for shorter scattering lengths ($<d_{B(M)}$). Thus, the measured Raman signal is corrected for the effective depth of pumping and collection and for the reflection losses at the air–slide or air–sample interfaces as:

$$I_{Exp(Al_2O_3,Glass,Air)} = I_{Exp} \times \left[\frac{l_s}{d_{B(M)}}\left(e^{-\frac{d_{B(M)}}{l_s}} - 1\right)\right]^{-2} \left\langle 1 - Ref_{CM}{}^{-1}\right\rangle \quad (1)$$

In eqn (1), $I_{Exp(Al_2O_3,Glass,Air)}$ is the corrected Raman signal. $d_{B(M)}$ and Ref_{CM} are the depth of pumping and collection for each slide and the reflection coefficient averaged over the pumping and collection cone angle at the air–slide or air–sample interfaces, respectively (see the ESI†).

For the above three setups (air, glass slide and sapphire slide), presented in Fig. 1, the Raman signal for each $FF_{TiO_2} > 0.26\%$, corrected by the effective depth of pumping and collection as well as by the reflected light at the air–slide or air–sample interfaces ($I_{Exp(Al_2O_3,Glass,Air)}$), was normalized by FF_{TiO_2} and the Raman signal at $FF_{TiO_2} = 0.26\%$ which allows the determination of the corrected Raman enhancement at each FF_{TiO_2}. For the above three setups, the determined-corrected Raman enhancement was plotted as a function of FF_{TiO_2} as presented in Fig. 2e and f. For the three arrangements and $FF_{TiO_2} < 4.8\%$, the corrected Raman enhancement at $FF_{SiO_2} = 1.5\%$ is stronger than that at $FF_{SiO_2} = 0.75\%$. This behavior is reverted for $FF_{TiO_2} \geq 4.8\%$, which has been explained in our recent previous work[4] through an increase of the residual absorption effect associated with the silica NPs ($FF_{TiO_2} \geq 4.8\%$). For all FF_{TiO_2} with both 0.75% and 1.5% FF_{SiO_2}, the lowest Raman enhancement was observed for the measurements without a slide (air), which can be explained through the collection losses due to internal reflection and light refraction at the sample–air interface caused by the enhanced refractive index of the sample near the sample–air interface. Additionally, for $FF_{TiO_2} < 1.35\%$, the strongest Raman enhancement was observed for the measurements with the sapphire slide. However, for $FF_{TiO_2} \geq 4.8\%$ with both 0.75% and 1.5% FF_{SiO_2}, the strongest Raman enhancement was achieved by using the glass slide. For $FF_{TiO_2} = 1.35\%$, Raman enhancements are similar for the measurements with both sapphire and glass slides. This result can be explained by the refractive index matching at the sample–slide (air, glass or sapphire) interfaces, which could be evidence of the dynamics of the effective refractive index in the sample interface. An index matching at the sample–slide interface reduces the collection losses by both the internal reflection and the decrease of the

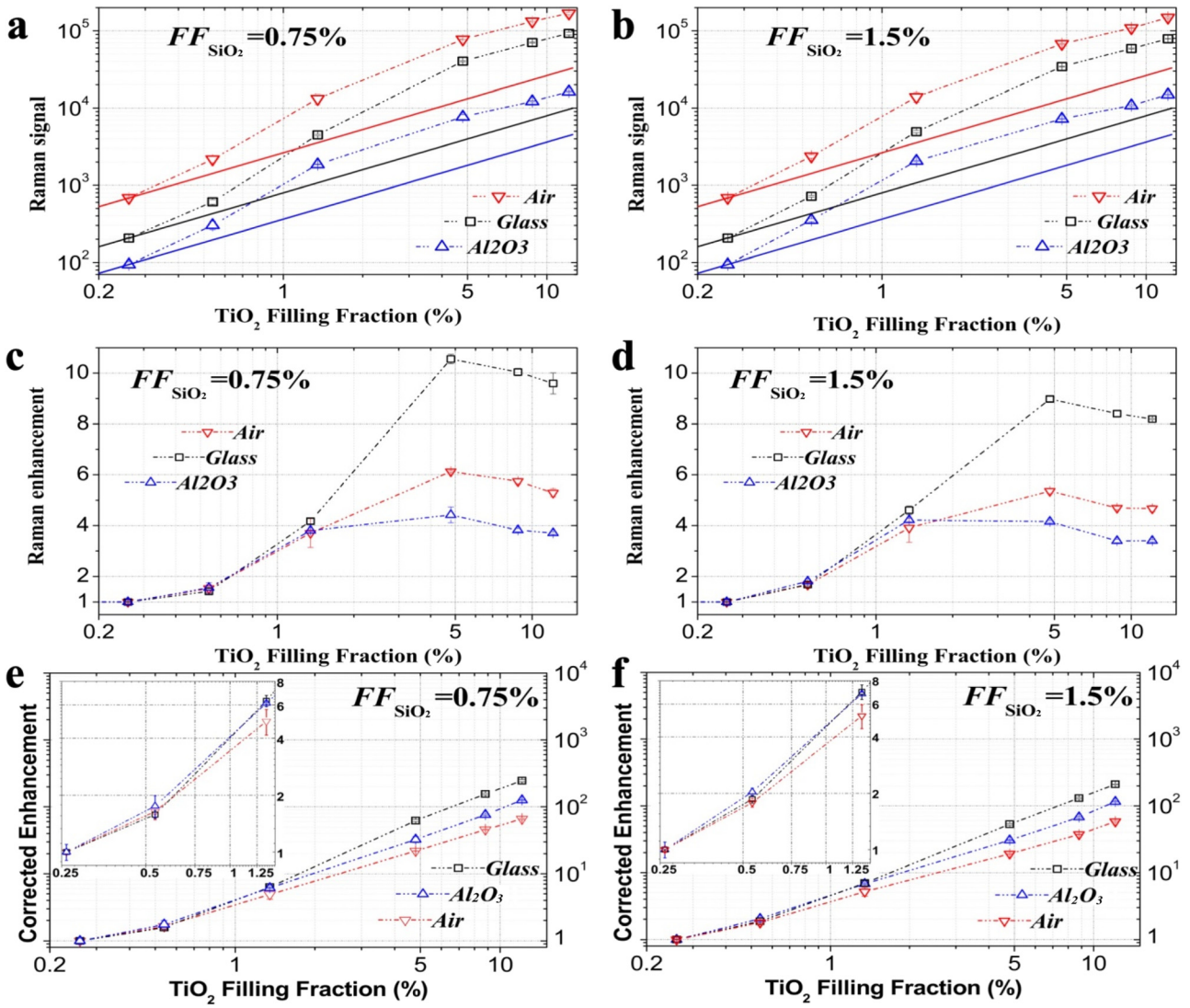

Fig. 2 Comparison of the Raman signal and Raman enhancements measured with the three setups (sapphire slide, glass slide and air). For the three arrangements, Raman signals for the samples with FF_{SiO_2} = 0.75% (a) are stronger than those with FF_{SiO_2} = 1.5% (b). Measured Raman enhancements for the samples with FF_{SiO_2} = 0.75% (c) and FF_{SiO_2} = 1.5% (d). The corrected Raman enhancements at FF_{SiO_2} = 0.75% (e) and FF_{SiO_2} = 1.5% (f) are higher than two orders for arrangements using glass and sapphire slides. The inset shows a zoomed-in view of the first three FF_{TiO_2} (0.26, 0.54 and 1.06%).

collection cone angle by light refraction at the sample–slide interface.

Next, in order to determine the losses by a possible n_S enhancement, for each $FF_{TiO_2} > 0.26\%$, a scaling or normalization factor was calculated for the glass slide ($I_{0.26\%(Glass)}/I_{Exp(Glass)}$), where $I_{0.26\%(Glass)}$ and $I_{Exp(Glass)}$ are the corrected Raman signals obtained with the glass slide for FF_{TiO_2} = 0.26% and $FF_{TiO_2} > 0.26\%$, respectively. The Raman signals measured at the lowest sample concentration, FF_{TiO_2} = 0.26%, was taken as a reference because there was no Raman signal enhancement[4] and presumably there should be no n_S enhancement either. We have taken as a reference the ratio of the Raman signals between FF_{TiO_2} = 0.26% and $FF_{TiO_2} > 0.26\%$ measured with the glass slide because the classical refractive indexes of the sample (n_{CS}) and glass slide (n_{CGlass}) are very close. Therefore, if we preliminarily assume that a similar n_{Glass} enhancement would also be induced at the sample–glass interface due to the interaction with the evanescent wave, the enhanced n_S and n_{Glass} at the sample–glass interface would also be very close. Thereby, the Raman signal losses due to the enhancement of the effective refractive indexes at the sample–glass interface (n_S and n_{Glass}) would be minimal. Clearly, the intensity of the evanescent wave decreases as it penetrates in the glass slide from the sample–slide interface. But as a first approximation, we will consider a similar enhancement of the electrical susceptibility of the glass (χ_{eGlass}) and the sample (χ_{eS}). With this normalization factor, we can obtain the expected values of the Raman signal enhancement if there

were no losses due to the refractive index enhancement using the equation:

$$I_{RS(Al_2O_3,Glass,Air)} = \frac{I_{Exp(Al_2O_3,Glass,Air)} \times I_{0.26\%(Glass)}}{I_{Exp(Glass)}} \quad (2)$$

where ($I_{RS(Al_2O_3,Glass,Air)}$) values will be used later. For each slide or air, the cone angle of the emitted-collected Raman signal, coming from the sample before refraction at the sample–slide or sample–air interfaces (θ_{SM}; θ_{SAir}, θ_{SGlass}, $\theta_{SAl_2O_3}$), must be linked to θ_{CM} (θ_{CAir}, θ_{CGlass}, $\theta_{CAl_2O_3}$), as shown in Fig. 1, using the following Snell expression:

$$n_S \sin\theta_{SM} = n_M \sin\theta_{CM} \Rightarrow \theta_{SM} = \sin^{-1}\left(\frac{n_M \sin\theta_{CM}}{n_S}\right) \quad (3)$$

where n_S and n_M are the effective refractive indexes of the sample and slide at the sample–slide interface, respectively. θ_{SM} without n_S enhancement (θ_{CS}) can be determined by evaluating the classical values of refractive indexes of the sample (n_{CS}) and slide (n_{CM}) in the above equation (eqn (3)). θ_{CS} can be determined as:

$$\theta_{CS} = \sin^{-1}\left(\frac{n_{CM} \sin\theta_{CM}}{n_{CS}}\right) \quad (4)$$

Thereby, we can estimate a classical value of the cone angle of the collected Raman signal from the sample without n_S enhancement (θ_{CS}). For FF_{TiO_2} = 4.8% and FF_{SiO_2} = 0.75%, if we consider n_{CS} = 1.44 and $\theta_{CAir} \approx 33.4°$ (air, without slides), θ_{CS} can be determined as follows:

$$\theta_{CS} \approx \sin^{-1}\left(\frac{\sin 33.4°}{1.44}\right) \approx 22.5°$$

This classical $\theta_{CS} \approx 22.5°$ (without enhancement) is the same for all microscope slides and air at FF_{TiO_2} = 4.8% and FF_{SiO_2} = 0.75% and only changes as a function of FF_{TiO_2}.

n_{CAir} = 1 remains constant even if the effective refractive index of the sample is enhanced (bigger than its classical index, $n_S > n_{CS}$). This is because the electric susceptibility of air is very close to zero, so its enhanced electric susceptibility must also be close to zero. However, θ_{SAir} would be lower than θ_{CS}, so a decrease in the collected Raman signal is expected. For $FF_{TiO_2} > 0.26\%$, the $I_{Exp(Air)}$ values are scaled as described by eqn (2), obtaining $I_{RS(Air)}$ values. The ratio ($I_{0.26\%(Air)}/I_{RS(Air)}$) = F_{Air} is defined as the deviation factor for the measurement without a slide (air). Note that F_{Air} is the ratio between the expected enhancement (if there were no losses in the collection) and the measured enhancement of the Raman signal, *i.e.*, F_{Air} represents the losses of collected Raman intensity (eqn (5)).

$$F_{Air} = \frac{I_{0.26\%(Air)}}{I_{RS(Air)}} = \frac{I_{0.26\%(Air)}}{I_{Exp(Air)}} \times \frac{I_{Exp(Glass)}}{I_{0.26\%(Glass)}} = \frac{1}{\text{Meas Enh.}} \times \text{Exp. Enh.} \quad (5)$$

Note that ($I_{Exp(Glass)}/I_{0.26\%(Glass)}$) represents the expected enhancement of the Raman signal for each $FF_{TiO_2} > 0.26\%$, as it was preliminarily assumed that there are no Raman collection losses using a glass slide. On the other hand, the collected Raman intensity (I_{CR}) is proportional to the total emitted Raman signal (I_{Te}) in the θ_{SM} cone angle, *i.e.*, $I_{CR} \propto I_{Te}(\theta_{SM})$ in the θ_{SM} cone angle. $I_{Te}(\theta_{SM})$ can be estimated by considering that the emitted Raman signal (I_{eR}) is a Lambertian function in the emission angle θ ($I_{eR}(\theta) \propto I_{e0}\cos\theta$), where I_{e0} is a constant that is proportional to the effective pumping intensity.

$$I_{Te}(\theta_{SM}) \propto 2\pi I_{e0} \int_0^{\theta_{SM}} \cos\theta d\theta \quad (6)$$

Integrating it, we have:

$$I_{Te}(\theta_{SM}) \propto 2\pi I_{e0} \int_0^{\theta_{SM}} \cos\theta d\theta = 2\pi I_{e0} \sin\theta_{SM} \Rightarrow I_{Te}(\theta_{SM}) \propto I_{e0} \sin\theta_{SM} \Rightarrow \frac{\text{Exp. Enh.}}{\text{Meas. Enh.}} = \frac{\sin\theta_{CS}}{\sin\theta_{SM}} = F_{Air} = \frac{I_{0.26\%(Air)}}{I_{RS(Air)}} \quad (7)$$

In this way, θ_{SM} for the measurement without a slide (θ_{SAir}) can be estimated using the following expression:

$$F_{Air} = \frac{\sin\theta_{CS}}{\sin\theta_{SAir}} \Rightarrow \theta_{SAir} \approx \sin^{-1}\left(\frac{\sin\theta_{CS}}{F_{Air}}\right) \quad (8)$$

Applying the Snell equation for this maximum angle of collection coming from the sample (θ_{SAir}) and assuming n_{Air} = 1, we obtain:

$$n_S \sin\theta_{SAir} = n_{CAir} \sin 33.4° \Rightarrow n_S = \frac{\sin 33.4°}{\sin\left(\sin^{-1}\left(\frac{\sin\theta_{CS}}{F_{Air}}\right)\right)} = \frac{F_{Air} \sin 33.4°}{\sin\theta_{CS}} \quad (9)$$

where $\theta_{CAir} = 33.4°$ is the half collection cone angle (see Fig. 1). In the above consideration, we did not introduce the losses by internal reflection at the sample–air interface (R_{SAir}), which can be estimated using Fresnel equations considering this enhanced refractive index, n_S, which has been preliminarily determined. $\langle R_{SAir}\rangle$ is the average loss by internal reflection on the collection cone (between 0° and θ_{SAir}) from the sample. Thereby, the more accurate n_S value can be estimated as follows:

$$n_S = \frac{F_{Air}\langle 1 - R_{SAir}\rangle \sin 33.4°}{\sin(\theta_{CS})} \quad (10)$$

From this n_S value, $\langle R_{SAir}\rangle$ is again determined, and a more accurate n_S value is again calculated by iteration, until n_S tends to reach the same value between iterations. We remark that the n_S value has been determined by considering that, for the measurement with a glass slide, there is no deviation between the expected and measured Raman enhancements, *i.e.*, $I_{0.26\%(Glass)}/I_{RS(Glass)}$ value is equal to unity, which was justified by assuming a similar enhancement for n_S and n_{Glass} at the

sample–slide interface. But the latter approximation was used in order to estimate a preliminary n_S value.

From this enhanced n_S value, the enhanced value of $n_{Al_2O_3}$, induced by the interaction with the evanescent wave at the sample–sapphire interface, can be estimated through the deviation factor with a sapphire cover slide, $F_{Al_2O_3} = (I_{0.26\%(Al_2O_3)}/I_{RS(Al_2O_3)})$. $\theta_{SAl_2O_3}$ can be expressed by applying a similar equation to eqn (8), substituting F_{Air} by $F_{Al_2O_3}$:

$$\theta_{SAl_2O_3} \approx \sin^{-1}\left(\frac{\sin\theta_{CS}}{F_{Al_2O_3}}\right) \tag{11}$$

Applying the Snell equation for this maximum angle of collection from the sample ($\theta_{SAl_2O_3}$), we obtain:

$$\begin{aligned} n_S \sin\theta_{SAl_2O_3} &= n_{Al_2O_3}\sin\theta_{CAl_2O_3} \\ n_{Al_2O_3} &= \frac{n_S\sin\theta_{CS}}{F_{Al_2O_3}\sin 18^\circ} \end{aligned} \tag{12}$$

where $\theta_{CAl_2O_3} = 18^\circ$ is the cone angle of pumping and collection on the sapphire cover slide (see Fig. 1). From this preliminarily calculated $n_{Al_2O_3}$ value, the average losses by internal reflection at the sample–sapphire interface ($\langle R_{SAl_2O_3}\rangle$) can be estimated using Fresnel's equations. Thereby, the more accurate $n_{Al_2O_3}$ value can be estimated as follows:

$$n_{Al_2O_3} = \frac{n_S\sin\theta_{CS}}{F_{Al_2O_3}\langle 1 - R_{SAl_2O_3}\rangle\sin 18^\circ} \tag{13}$$

From this $n_{Al_2O_3}$ value, $\langle R_{SAl_2O_3}\rangle$ was again determined, and a more accurate $n_{Al_2O_3}$ value was again calculated by iteration, until $n_{Al_2O_3}$ tends to reach the same value between iterations. It is important to remark again that in the latter considerations we assumed as a first approximation that n_{Glass} at the sample–glass interface undergoes an enhancement similar to that of the sample. However, the effective refractive index and susceptibility of the slide should decrease progressively from the sample–slide interface since the interaction of the evanescent wave decreases as it penetrates in the glass slide. This implies that the effective enhancement of susceptibility of the slide at the sample–glass interface should be less than that of the sample. The effective n_{Glass} value (enhanced) at the sample–glass interface can be estimated theoretically from the enhanced $n_{Al_2O_3}$ value determined above. Assuming that the classical susceptibilities of glass ($\chi_{eCGlass}$) and sapphire ($\chi_{eCAl_2O_3}$) at the sample–slide interface should be enhanced approximately equally, the enhanced n_{Glass} can be estimated as:

$$\begin{aligned} n_{Glass} &= \sqrt{1+\chi_{eGlass}} \\ n_{Glass} &= \sqrt{1+\left(\frac{\chi_{eAl_2O_3}}{\chi_{eCAl_2O_3}}\right)\chi_{eCGlass}} \end{aligned} \tag{14}$$

where $\chi_{eAl_2O_3}$ and χ_{eGlass} are the enhanced susceptibilities of sapphire and glass at the sample–slide interface, respectively. From the enhanced n_{Glass} value, above calculated, we can estimate the glass deviation factor (F_{Glass}) for each FF_{TiO_2} and FF_{SiO_2}, and then apply the Snell equation for this maximum angle of collection from the sample using the glass slide (θ_{SGlass}) and apply eqn (7) for F_{Glass}:

$$\begin{aligned} n_S\sin\theta_{SGlass} &= n_{Glass}\sin\theta_{CGlass} \Rightarrow \\ \theta_{SGlass} &= \sin^{-1}\left(\frac{n_{Glass}\sin 21.2^\circ}{n_S}\right) \Rightarrow \\ F_{Glass} &= \frac{\sin\theta_{CS}}{\sin\theta_{SGlass}} = \frac{n_S\sin\theta_{CS}}{n_{Glass}\sin 21.2^\circ} = \frac{I_{0.26\%(Glass)}}{I_{RS(Glass)}} \end{aligned} \tag{15}$$

where $\theta_{CGlass} = 21.2^\circ$ is the collection cone angle on the glass cover slide (see Fig. 1). Note that θ_{CS} is only determined by FF_{TiO_2}. From the F_{Glass} values and eqn (2) and (5), new corrected values of $F'_{Air} = (F_{Air}/F_{Glass})$ and $F'_{Al_2O_3} = (F_{Al_2O_3}/F_{Glass})$ were obtained. Consecutively, n_S, $n_{Al_2O_3}$ and n_{Glass} values were again calculated (more accurately) from F'_{Air} and $F'_{Al_2O_3}$ values. Fig. S3 (ESI†) shows a schematic diagram of the flow of operations to determine the effective refractive indexes of the sample and slides (n_S, $n_{Al_2O_3}$ and n_{Glass}) at the sample–slide interface.

Fig. 3a and b show the effective refractive indexes (n_S) and electric susceptibilities (χ_{eS}) of the samples, experienced by emitted Raman photons, at the input sample–slide interface, extracted using the above method, as a function of FF_{TiO_2}, respectively.

A monotonic n_S and χ_{eS} increase is observed as FF_{TiO_2} is increased. For all FF_{TiO_2}, the effective refractive index and electric susceptibility of the samples with $FF_{SiO_2} = 1.5\%$ are higher than those of the samples with $FF_{SiO_2} = 0.75\%$. This behavior is expected for $FF_{TiO_2} < 4.8\%$, since Raman enhancement for $FF_{TiO_2} < 4.8\%$ is stronger in the samples with $FF_{SiO_2} = 1.5\%$, (stronger enhanced Raman signal) in comparison with the samples with $FF_{SiO_2} = 0.75\%$ (Fig. 2). However, for $FF_{TiO_2} \geq 4.8\%$, the above behavior is not intuitive since the enhanced Raman signal is larger for the samples with $FF_{SiO_2} = 0.75\%$. This may be the result of a higher residual absorption in the samples with $FF_{SiO_2} = 1.5\%$ (larger total surface area of SiO_2 NPs),[4] which for $FF_{TiO_2} \geq 4.8\%$ would begin to contribute appreciably to the value of the deviation factors used to calculate the effective refractive index. This effect would be particularly pronounced for the F_{Air} values, due to the higher internal reflection (higher refractive index contrast) at this sample–air interface. For $FF_{TiO_2} \geq 4.8\%$, the collected Raman signal can be reduced (mainly in air) by two main causes: (i) the decrease of the collection cone angle due to the refraction of light at the sample–slide interface (approximation used for the refractive index determination) and (ii) a more strongly enhanced residual absorption (particularly, for the samples with $FF_{SiO_2} = 1.5\%$). The latter hypothesis would imply that the F_{Air} value includes implicitly additional losses by residual absorption ($FF_{TiO_2} \geq 4.8\%$), which means that the F_{Air} value, extracted from the measurements and used for refractive index determination, would be effectively increased by the residual absorption (mainly for $FF_{SiO_2} = 1.5\%$ and $FF_{TiO_2} \geq 4.8\%$). The latter would limit the accuracy of the above method to only a negligible residual absorption.

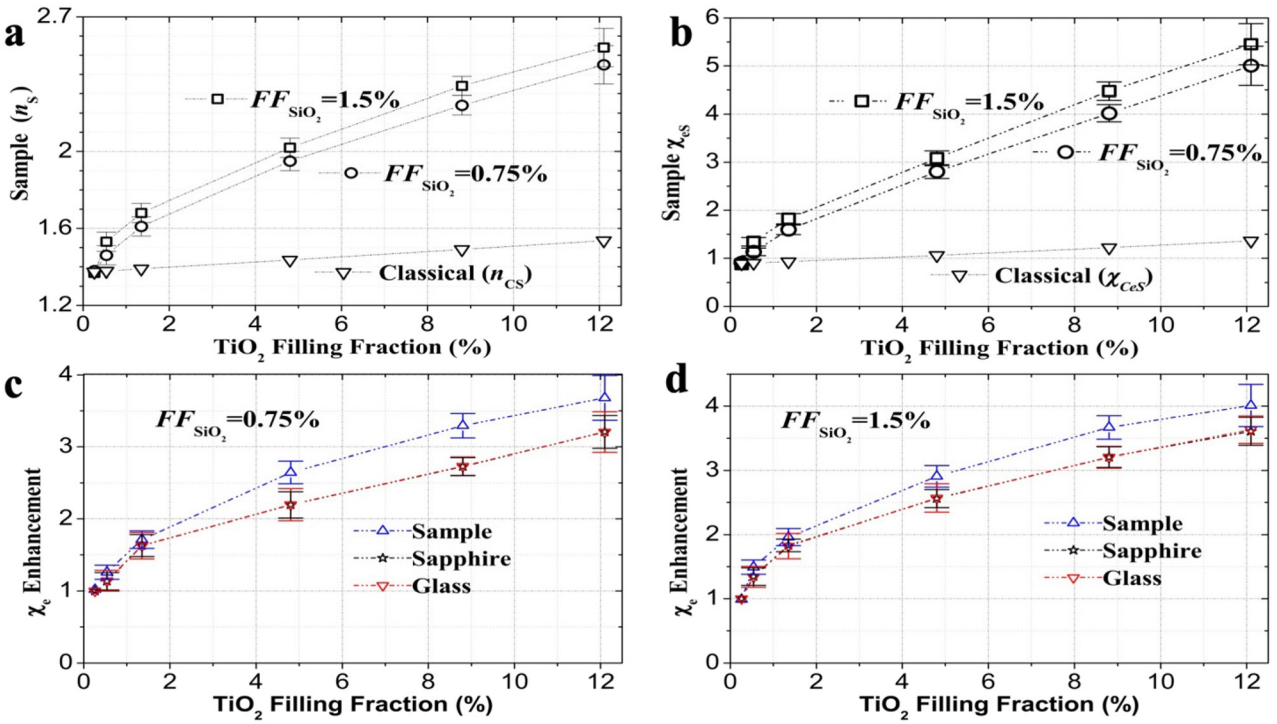

Fig. 3 Determination of the effective refractive index and the corresponding electric susceptibilities extracted by the losses of the Raman signals. (a) Strong enhancement of the effective refractive index (n_S) and (b) electric susceptibility (χ_{eS}) of the sample is observed as FF_{TiO_2} is increased. Black inverted triangles in (a) represent the classical refractive index (n_{CS}) and in (b) represent the classical electric susceptibility (χ_{CeS}) of the sample calculated by Maxwell–Garnett approximation; (c and d) electric susceptibility enhancements of the samples (blue triangles), sapphire (black stars) and glass (red triangles) extracted from measurements using samples with FF_{SiO_2} = 0.75% (c) and FF_{SiO_2} = 1.5% (d).

Fig. 3c and d show the enhancement of the electric susceptibilities (sample, sapphire and glass) experienced by Raman photons and extracted from the measurements in the samples with 0.75% and 1.5% FF_{SiO_2}, respectively. For all FF_{TiO_2}, the enhancements of the effective susceptibilities (sample, sapphire and glass) for FF_{SiO_2} = 1.5% are stronger than for FF_{SiO_2} = 0.75%. Again, for the samples with $FF_{TiO_2} \geq 4.8\%$ and FF_{SiO_2} = 1.5%, this may be due to a higher loss of the Raman signal given its higher residual absorption. Additionally, for both FF_{SiO_2}, the enhancement of the slide's susceptibilities (sapphire and glass slides) is less than that of the sample's, which can be explained by the decrease of the evanescent wave interaction coming from the sample entering the slides.

The extended enhancement of the effective refractive index to the immediate vicinity of the sample edge through interaction with the evanescent wave coming from the sample represents a phenomenon to highlight that makes it a powerful sensing tool with great potential applications. It should be noted that different from the SERS phenomenon, where strong enhancement of light–matter coupling occurs very close to the nanometallic structure and at a specific wavelength and bandwidth (plasmon resonance),[28] the strong enhancement of the effective refractive index, described in this work, is extended to longer distances from the sample surface (extension of the evanescent wave) and possibly to a wider range of wavelengths (see our previous work).[4] This means that the evanescent wave extension range in the near vicinity of the medium is considerably larger (hundreds of nanometers) than that of SERS (several nanometers).

For a negligible residual absorption, the enhancement factor of the sample's electric susceptibility, $G_{\chi e}$, experienced by the Raman photons is:

$$G_{\chi e} = \frac{E_{Loc}(\omega_R)}{E_0(\omega_R)}$$

where E_{Loc} is the locally enhanced electromagnetic field resulting from recurrent scattering in effective cavities at the Raman emission frequency (ω_R) and E_0 represents the electromagnetic field of the Raman emission. This is a linear dependence of the susceptibility enhancement, experienced by the Raman photons, with the enhancement of the Raman electromagnetic field trapped in strongly localized electromagnetic modes (effective cavities).

On the other hand, the enhancement factor of the Raman signal (G_R) due to strongly localized electromagnetic field is defined as:

$$G_R = \frac{|E_{Loc}(\omega_P)|^2}{|E_0(\omega_P)|^2} \times \frac{|E_{Loc}(\omega_R)|^2}{|E_0(\omega_R)|^2} \approx \frac{|E_{Loc}(\omega_P)|^2 \times |E_{Loc}(\omega_R)|^2}{|E_0|^4}$$

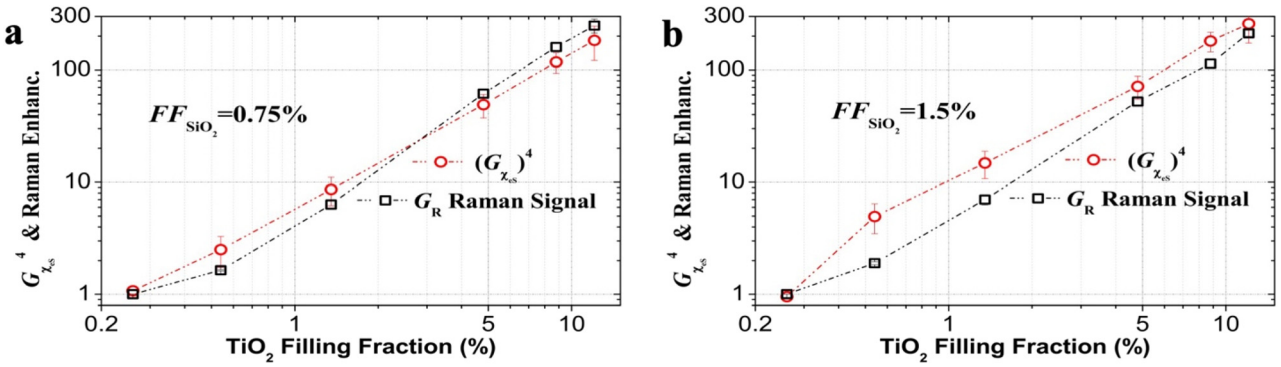

Fig. 4 Comparison of the Raman enhancement measured using a glass slide to cover the samples, G_R (black open squares), and fourth power of the electric susceptibility enhancement, $(G_{\chi e})^4$ (red open circles), for the samples with (a) FF_{SiO_2} = 0.75% and (b) FF_{SiO_2} = 1.5%.

where ω_P and ω_R are the pumping and emission Raman frequencies, respectively. E_{Loc} is the locally enhanced electromagnetic field resulting from recurrent scattering in effective cavities, at the pumping (ω_P) and emission Raman (ω_R) frequencies. $E_0(\omega_P)$ and $E_0(\omega_R)$ represent the electromagnetic field of the incoming laser wave (pumping) and the Raman emission, respectively. If $\omega_P \approx \omega_R$, the scattering strength could be considered to be approximately the same for both electromagnetic waves and a fourth power dependence of the Raman signal enhancement is expected. In this way, if similar enhancements of locally confined electromagnetic fields are assumed for pumping (ω_P) and Raman emission (ω_R) frequencies, then $(G_{\chi e})^4 \approx G_R$. Clearly, the coherence of Raman emission is lower than that of the Raman pump laser, which could reduce the confinement for the Raman emission. Consequently, the electromagnetic field enhancement of the Raman emission would be less than that experienced by the Raman pump laser.

For the glass slide arrangement, Fig. 4a and b show a comparison of the Raman enhancement (G_R) and the fourth power of the electrical susceptibility enhancement $(G_{\chi e})^4$ for the samples with FF_{SiO_2} = 0.75% and FF_{SiO_2} = 1.5%, respectively. For FF_{SiO_2} = 0.75% (Fig. 4a), where the residual absorption effect should show less influence, a similar monotonic increase of G_R and $(G_{\chi e})^4$ in FF_{TiO_2} (seemingly a power law) is observed. Nevertheless, $(G_{\chi e})^4$ increase is slightly lower (lower slope) than G_R increase for $FF_{TiO_2} \geq 4.8\%$. The latter could be a consequence of a decrease in light confinement for Raman emission in comparison with the Raman pumping source, due to the low coherence of the Raman emission.

For FF_{SiO_2} = 1.5% (Fig. 4b), a similar monotonic increase of G_R and $(G_{\chi e})^4$ in FF_{TiO_2} is also observed. Nevertheless, $(G_{\chi e})^4$ values are slightly higher than G_R values, which could be attributed to the effect of residual absorption. Note that the residual absorption should contribute for both a decrease of the Raman enhancement and an increase of the electrical susceptibility enhancement.

It is important to highlight that this enhancement of the effective refractive index at the sample–slide interface, experienced by Raman photons, is experienced for the Raman emission intensity that is much lower than the Raman pumping intensity. Taking into account the nonlinear refractive index coefficient recently reported for rutile films ($n_2 = -1.36 \times 10^{-16}$ m^2 W^{-1})[29] and the power densities used for pumping ($\sim 10^{11}$ W m^{-2}), both for a wavelength of 532 nm, the variation of refractive index (Δn rutile) must be around $\Delta n \sim -10^{-5}$. This further suggests that the observed enhancement of the effective refractive index experienced by the Raman emission (power density several orders lower) represents an anomalous non-linear phenomenon that cannot be explained in the context of the classical nonlinear optical framework, *i.e.*, it would be essentially and conceptually different from a classical non-linear phenomenon.

Contrary to a classical non-linear phenomenon, which is due to the increased probability of simultaneous multi-photon interaction (very strong electromagnetic field), we propose that this anomalous non-linear phenomenon would be induced by the increased probability of sequential photon interactions, due to the strong correlation of the photons in the strongly localized electromagnetic modes. The latter can be understood as successive polarization of valence electrons to virtual states. The considerable benefit of sequential photon interaction is that it emerges even at very low intensity of the incoming electromagnetic field, *i.e.*, there is no threshold for this phenomenon.

Further studies on the enhancement of the Raman signal and refractive index in this correlated-structured scattering system are called for in order to deepen the understanding on these strongly localized electromagnetic modes (localization of light) and associated phenomena.

Conclusion

By studying the Raman signal in this structured scattering medium with three configurations (two different cover slides and air), the effective refractive indexes of the structured medium (sample) and slides (sapphire and glass) experienced by Raman photons at the sample–slide interface were extracted. A strong enhancement of the effective refractive index experienced by the Raman photons is determined. This

finding is attributed to the electromagnetic modes strongly localized in this structured scattering medium and the evanescent wave interaction coming from them, whose origin is induced by the correlation in the scatterers' position. The latter is caused by a strong Coulomb interaction between TiO_2@Silica NPs (scatterers), which is favored by the presence of silica NPs of 20 nm size. The silica NPs act like pivots or bridges for the interaction between TiO_2@Silica NPs, leading to a stronger correlation in the scatterers' positions which, in turn, favors interferential processes (higher density and *Q*-factors of strongly localized electromagnetic modes).

The enhancement of the effective refractive index of both sapphire and glass slides, due to the evanescent wave interaction, is weaker than that of the sample, which is explained through the decrease of the evanescent wave interaction coming from the sample entering the slides. This strong enhancement of the effective refractive index, extended to the vicinity of loss-less materials, opens up a number of interesting sensing applications that require extended volumes of interaction and spectral sensitivities, which are way outside the SERS capabilities. A study of the detection sensitivity of molecules immobilized on a solid interface in contact with this structured medium is called for in order to demonstrate possible applications. The findings presented here open an avenue for designing and manufacturing advanced photonics devices.

Author contributions

F.C.M. & E.J.V. synthesized the nanoparticles; J.D., N.U.W. & E. J.V. performed the Raman experiments; J.D., N.U.W., F.C.M., A.D. & E.J.V. analyzed the results and prepared the manuscript; E.J.V. wrote the manuscript and guided the research.

Data availability

Data for this article, including collected Raman signals for each experimental arrangement and concentrations of TiO_2@Silica and silica NPs, are available at the following link: **https://drive.google.com/drive/folders/1VqnzGWPZPumwiIMeqFd-SvNBbO1U5WQv?usp=sharing**.

Conflicts of interest

The authors declare no conflicts of interest.

Acknowledgements

We gratefully acknowledge financial support from FAPESP (grants 2022/02525-2; 2019/06334-4; 2021/04334-7; 2017/11986-5 and 2017/10765-5), CNPq (grants 313703/2021-3, 435260/2018-9, 465423/2014-0) and IPEN/CNEN 2020.06.IPEN.33.PD. This work was partially funded by the Office of Naval Research under N00014-20-1-2789.

References

1 V. A. Ermakov, W. S. Martins, N. U. Wetter, F. C. Marques and E. Jiménez-Villar, *Nanoscale*, 2021, **13**, 6417–6425.
2 S. John, *Nat. Mater.*, 2012, **11**, 997–999.
3 S. John, *Phys. Today*, 1991, **44**, 32.
4 J. Dipold, N. Wetter, F. Marques, A. Freitas, A. Dogariu and E. Jimenez Villar, *J. Opt. Soc. Am. B*, 2024, **41**, 1415.
5 C. T. Dominguez, A. A. V. Gomes, N. U. Wetter, J. Dipold, V. Mestre, W. S. Martins and E. Jiménez-Villar, *Opt. Mater.*, 2021, **120**, 111428.
6 S. Torquato, *J. Compos. Mater.*, 2022, **56**, 3635–3649.
7 F. Sgrignuoli, S. Torquato and L. Dal Negro, *Phys. Rev. B: Condens. Matter Mater. Phys.*, 2022, **105**, 064204.
8 S. Yu, C.-W. Qiu, Y. Chong, S. Torquato and N. Park, *Nat. Rev. Mater.*, 2020, **6**, 226–243.
9 K. Vynck, R. Pierrat, R. Carminati, L. S. Froufe-Pérez, F. Scheffold, R. Sapienza, S. Vignolini and J. J. Sáenz, *Rev. Mod. Phys.*, 2023, **95**, 045003.
10 S. Yu, *Nat. Comput. Sci.*, 2023, **3**, 128–138.
11 P. A. Nosov, I. M. Khaymovich and V. E. Kravtsov, *Phys. Rev. B*, 2019, **99**, 104203.
12 D. S. Wiersma, P. Bartolini, A. Lagendijk and R. Righini, *Nature*, 1997, **390**, 671–673.
13 M. Störzer, P. Gross, C. M. Aegerter and G. Maret, *Phys. Rev. Lett.*, 2006, **96**, 1–4.
14 F. Scheffold and D. Wiersma, *Nat. Photonics*, 2013, **7**, 934.
15 F. Scheffold, R. Lenke, R. Tweer and G. Maret, *Nature*, 1999, **398**, 206–207.
16 T. Van Der Beek, P. Barthelemy, P. M. Johnson, D. S. Wiersma and A. Lagendijk, *Phys. Rev. B: Condens. Matter Mater. Phys.*, 2012, **85**, 1–11.
17 S. E. Skipetrov and J. H. Page, *New J. Phys.*, 2016, **18**, 021001.
18 S. John, *Phys. Rev. Lett.*, 1984, **53**, 2169–2172.
19 E. Jimenez-Villar, I. F. Da Silva, V. Mestre, P. C. De Oliveira, W. M. Faustino and G. F. De Sá, *Nanoscale*, 2016, **8**, 10938–10946.
20 K. Dutta and S. K. De, *J. Nanopart. Res.*, 2007, **9**, 631–638.
21 A. S. Dukhin and P. J. Goetz, in *Characterization of Liquids, Dispersions, Emulsions, and Porous Materials Using Ultrasound*, Elsevier, 2017, pp. 19–83.
22 E. Jimenez-Villar, V. Mestre, W. S. Martins, G. F. Basso, I. F. da Silva and G. F. de Sá, *Mater. Today: Proc.*, 2017, **4**, 11570–11579.
23 E. Jiménez-Villar, I. F. da Silva, V. Mestre, N. U. Wetter, C. Lopez, P. C. de Oliveira, W. M. Faustino and G. F. de Sá, *ACS Omega*, 2017, **2**, 2415–2421.
24 E. Jimenez-Villar, M. C. S. Xavier, J. G. G. S. Ramos, N. U. Wetter, V. Mestre, W. S. Martins, G. F. Basso, V. A. Ermakov, F. C. Marques and G. F. de Sá, in *Complex*

Light and Optical Forces XII, ed. D. L. Andrews, E. J. Galvez and J. Glückstad, SPIE, 2018, vol. 1054905, p. 4.
25 E. Jimenez-Villar, M. C. S. Xavier, N. U. Wetter, V. Mestre, W. S. Martins, G. F. Basso, V. A. Ermakov, F. C. Marques and G. F. de Sá, *Photonics Res.*, 2018, **6**, 929.
26 G. Campagnano and Y. V. Nazarov, *Phys. Rev. B: Condens. Matter Mater. Phys.*, 2006, **74**, 1–15.
27 E. Jiménez-Villar, W. S. Martins and N. U. Wetter, *Appl. Opt.*, 2023, **62**, 2707.
28 M. Jahn, S. Patze, I. J. Hidi, R. Knipper, A. I. Radu, A. Mühlig, S. Yüksel, V. Peksa, K. Weber, T. Mayerhöfer, D. Cialla-May and J. Popp, *Analyst*, 2016, **141**, 756–793.
29 H. Long, A. Chen, G. Yang, Y. Li and P. Lu, *Thin Solid Films*, 2009, **517**, 5601–5604.